Chapter 12

HRMA Effective Area: Spectral Line Measurements

Richard J. Edgar

12.1 Introduction

This chapter describes the best effort to date to reduce data taken to determine the on-axis effective area of the HRMA shells. These experiments consist of electron impact point source (EIPS) measurements done in Phase 1, with flow proportional counters (FPC) and solid state detectors (SSD) used as both beam normalization detectors and at the HRMA focal point. In principle, since all the detectors of each type are nearly identical, most of the detector effects will cancel. In practice, at the few percent level, no two physical artifacts are identical, and so we will need to calibrate a great many effects and carefully remove them from the data.

12.2 FPC Data Reduction

The data were processed in much the same way as the generic XRCF FPC data, as described in §9.4. In order to improve the fidelity of the analysis, however, certain systematic effects need to be accounted for, which necessitates additional care in some aspects of the data reduction.

One such effect is to include the (rough) shape of the HRMA effective area curve in the analysis. Since the input spectrum is a strong line with a weak continuum, the main effect of modulating the spectrum with the HRMA effective area (as a function of energy) is to change the shape of the continuum. This does not change the counting rate at the line, but rather the shape of the continuum. Fitting the continuum well allows one to confidently separate continuum photons that fall in the region of the line from line photons, and to quote a counting rate due to line photons only, despite the poor intrinsic resolution of the FPC detectors.

Most of the tests covered here are encircled energy (EE) tests, which have many iterations using different sizes of pinhole apertures on the focal plane detector. After verifying that the counting rates measured by the BND-H detectors are time-independent to within 1.5% (often within 0.3%), the data from all these iterations (or those where a given detector was functioning, if it went offline for some of them) were co-added, to improve the signal to noise ratio for further analysis. In one case, Cr K–α, the beam flux was decaying monotonically with time, so we did not co-add the BND

Instr.	Line	E (keV)	Shell	TRW ID	Runid 35mm	Runid 2mm
FPC	C−Kα	0.277	1	D−IXF−EE−3.001	108597	108593
FPC	C−Kα	0.277	1	D−IXF−EE−3.012	108549	108545
FPC	C−Kα	0.277	3	D−IXF−EE−3.002	108627	108623
FPC	C−Kα	0.277	3	D−IXF−EE−3.013	108572	108568
FPC	C−Kα	0.277	4	D−IXF−EE−3.003	108658	108654
FPC	C−Kα	0.277	4	E−IXF−EE−3.014	110488	110484
FPC	C−Kα	0.277	6	D−IXF−EE−3.004	108689	108685
FPC	C−Kα	0.277	6	E−IXF−EE−3.015	110518	110513
FPC	Cu−Lα	0.930	all	D−IXF−EE−4.002	109397	109393
FPC	Al−Kα	1.486	1	D−IXF−EE−2.001	107326	107321
FPC	Al−Kα	1.486	3	D−IXF−EE−2.002	107358	107354
FPC	Al−Kα	1.486	4	D−IXF−EE−2.003	107388	107384
FPC	Al−Kα	1.486	6	D−IXF−EE−2.004a	107979	107975
SSD	Nb−Lα	2.166	all	D−IXS−MC−1.001	...	110126
SSD	Ag−Lα	2.980	all	E−IXS−EE−71.001	...	111193
SSD	Sn−Lα	3.444	all	D−IXS−EE−99.021	...	110097
FPC	Ti−Kα	4.510	1	D−IXF−EE−3.005	109125	109121
FPC	Ti−Kα	4.510	3	D−IXF−EE−3.006	109221	109217
FPC	Ti−Kα	4.510	4	D−IXF−EE−3.007	109157	109153
FPC	Ti−Kα	4.510	6	D−IXF−EE−3.008	109187	109183
FPC	Ti−Kα	4.510	all	D−IXF−3D−9.001	...	109242
FPC	Cr−Kα	5.410	all	E−IXF−EE−4.004	111904	111900
FPC	Fe−Kα	6.400	3	D−IXF−EE−3.009A	108232	108228
FPC	Fe−Kα	6.400	4	D−IXF−EE−3.010a	108350	108346
FPC	Fe−Kα	6.400	6	D−IXF−EE−3.011	108298	108294
FPC	Cu−Kα	8.030	all	D−IXF−EE−4.001	109360	109356

Table 12.1: Encircled Energy tests analyzed for the HRMA effective area

spectra.
A few of the effects which can be corrected are:

- Gain Nonuniformity in the open BND-H detectors
- Relative Quantum Efficiencies (RQE) of the detectors
- Beam Uniformity (BU) effects

Each of these is described in detail below.

In Table 12.1 we list the TRW ID numbers for each of the encircled energy tests we have analyzed in this effort. The corrections involve data from other tests, such as background runs, beam uniformity tests, and flat field tests. We list in Table 12.2 the TRW ID numbers of these other ancillary tests.

12.3 Gain Nonuniformity in the open BND-H detectors

Unlike the fpc_5 and focal plane FPC detectors, the BND-H detectors have a substantial amount of open area, approximately 3.6 × 9.9 cm. The response of these single-wire flow proportional

Line	E(keV)	BG TRW ID	BU TRW ID	RBG TRW ID	RQE TRW ID
C−Kα	0.277	D−IXF−BG−1.019	D−BND−BU−2.038	J−IXF−BG−1.027a	J−BND−BU−2.038
Cu−Lα	0.930	D−IXF−BG−1.001	D−BND−BU−2.001	J−IXF−BG−1.001	J−BND−BU−2.002
Al−Kα	1.486	D−IXF−BG−1.018b	D−BND−BU−2.036a	J−IXF−BG−1.026a	J−BND−BU−2.036
Nb−Lα	2.166	D−IXF−BG−1.007	D−BND−BU−2.013	J−IXF−BG−1.007	J−BND−BU−2.013
Ag−Lα	2.980	E−IXF−BG−1.008	E−BND−BU−2.015	J−IXF−BG−1.008	J−BND−BU−2.015
Sn−Lα	3.444	D−IXF−BG−1.010	J−BND−BU−2.019	J−IXF−BG−1.010	J−BND−BU−2.019
Ti−Kα	4.510	D−IXF−BG−1.015	D−BND−BU−2.030	J−IXF−BG−1.024	J−BND−BU−2.030
Cr−Kα	5.410	E−IXF−BG−1.012	E−BND−BU−2.023	J−IXF−BG−1.012	J−BND−BU−2.024
Fe−Kα	6.400	D−IXF−BG−1.013	D−BND−BU−2.028	J−IXF−BG−1.023	J−BND−BU−2.028
Cu−Kα	8.030	D−IXF−BG−1.002	D−BND−BU−2.004	*I−IAI−SG−5.024	*I−BND−BU−2.004

Table 12.2: Ancillary tests used in the present analysis. *Since no flat field tests were done at Cu-Kα in phase J, these are from phase I. The relative quantum efficiency for fpc_hs is assumed to be equal to that of fpc_hb.

counters has been found to be quite uniform across the wire (in the Y direction at XRCF), but the gain is significantly higher near the ends of the detectors. Prior to the calibration, the blocking plate apertures were reworked, giving a somewhat smaller open area and masking the ends of the counters where the gain was largest. However, there is still enough variation of gain along the wire that it must be taken into account in order to obtain acceptable fits to the spectra.

The fpc_hn detector could be used either open, or with a 36 mm circular aperture. When used with the 36 mm aperture, the gain nonuniformity effect is negligible.

We have used a technique involving two interlinked `JMKmod` models to fit these data, in order to account for the gain nonuniformity in these detectors. This is described in detail in §9.4.

12.4 FPC Beam Uniformity (BU) effects

The x-ray beam produced by the electron impact point source (EIPS) at XRCF is quite uniform. Beam Uniformity tests (BU) were conducted at each energy, and so the few percent variations in intensity with position across the HRMA entrance can be accounted for. These experiments (see Chapter 24) consisted of moving the fpc_hn around in front of the HRMA entrance, and to the position of each of the BND-H detectors. We can then calculate a beam uniformity factor for each detector (or the average over a given part of the HRMA) by:

$$BU_{det} = R(\text{fpc\_hn at det})/R(\text{fpc\_5}),$$

where the R variables are (fitted) count rate fluxes in detector counts s^{-1} cm^{-2}, projected to the HRMA entrance plane. The normalization to the fpc_5 rate controls for possible time-dependence of the beam strength. In Chapter A, we list the aperture areas and source distances used in this reduction effort.

12.5 Relative Quantum Efficiencies (RQE) of the FPC detectors

Data from the Phase I and J flat field tests were analyzed to compute relative quantum efficiencies for the HXDS detectors. The results of the analysis of these data are summarized in §3.5.3.

These tests were conducted in much the same manner as the Beam Uniformity tests during the HRMA calibration. In this case, the fpc_hn was positioned in turn in front of each of the other

FPC detectors (the BND-H detectors, and the fpc_x2). Some of the exposures were done with the fpc_hn open, and some with the 36 mm circular aperture. Thus double `JMKmod` fits must be done to analyze these data. When the 36 mm aperture is in use, the norm of the second `JMKmod` fits to a very small fraction of the main model component. A beam uniformity factor can be computed for each detector position from the same flat field data (not to be confused with the BU factors from the main HRMA calibration, discussed above), and the relative quantum efficiency can be computed:

$$RQE_{det} = \frac{R_{det}}{R_{\text{fpc\_hn}}} \times \frac{BU_{\text{fpc\_hn}}}{BU_{det}}.$$

It is a worthwhile exercise to work through the units in this equation. The first ratio of R variables is in detector counts per fpc_hn count, measured at the fpc_hn home position. The BU factors are in fpc_hn counts at the home position, and at the position of the detector in question, respectively:

$$RQE_{det} \sim \frac{det \text{ counts}}{\text{fpc\_hn counts at home}} \times \frac{\text{fpc\_hn counts at home/fpc\_5 counts}}{\text{fpc\_hn counts at } det\text{/fpc\_5 counts}}.$$

Since the counters were operated at systematically different temperatures during the Phase 1 HRMA calibration and the Phase J flat field measurements, corrections have been made in accordance with the method described in §3.5.4. This amounts to less than 2% and is most important at high energies, and just below 3 keV. The effect arises because the pressure of the gas in the FPCs was controlled and quite stable at 400 torr, and so the density of the gas varies inversely as the absolute temperature. This in turn makes the optical depth of the gas vary, and so at high energies where this optical depth is not large, the quantum efficiency of the counters can be affected.

Note that no direct RQE measurement is available for fpc_hs at Cu K–α. We assume that the RQE for this detector is the same as for fpc_hb, which is true at other high energies (see Table 3.5).

12.6 Corrected HRMA Entrance Flux: FPC detectors

Now that we have corrections for beam uniformity and relative quantum efficiency, we can combine these with the BND data to compute a corrected flux at the HRMA entrance. Note that, since the QE corrections are relative to the fpc_hn, all corrected fluxes are in units of fpc_hn counts s^{-1} cm^{-2}. For each detector,

$$F_{det} = \frac{\langle BU_{HRMA} \rangle}{BU_{det}} \times \frac{R_{det}}{RQE_{det}},$$

where R_{det} is the count rate flux in the detector in question, in counts s^{-1} cm^{-2}, projected to the HRMA entrance plane. The quantity $\langle BU_{HRMA} \rangle$ is the average beam uniformity factor over the exposed portion of the HRMA.

The four corrected fluxes due to the four BND-H detectors are then averaged to give $\langle F \rangle$:

$$\langle F \rangle = \frac{1}{4} \sum_{BND} F_{BND}.$$

12.7 Effective Areas: FPC detectors

We then put the above corrections together to produce a number for the effective area of the HRMA at each energy for each mirror combination exposed.

$$A_{eff} = \frac{C_{\mathsf{fpc\_x2}}/RQE_{\mathsf{fpc\_x2}}}{\langle F\rangle},$$

where $C_{\mathsf{fpc\_x2}}$ is the count rate in the fpc_x2. Note that dividing by the RQE for this detector puts the numerator in units of fpc_hn counts s^{-1}, so that the effective area comes out in units of cm^2.

We give these values in Table 12.3 (for 35 mm apertures) and Table 12.4 (for 2 mm apertures). Also listed in the tables are the average BND fluxes, and various contributions to the error (see next section).

For comparison with ray trace models, we show the data derived here on plots of effective area vs. energy for each shell, and for the HRMA ensemble in Figures 12.1to12.6. The ray trace models shown here are those from model `xrcf_SA01G+HDOS_HDOS-scat-970220_03`, which is described in Chapter 10. The HRMA ensemble points at C, Al, Ti, and Fe K–α (0.277, 1.49, 4.51, and 6.4 keV) are sums of the single shell effective areas (assuming 4.1 and 4.7 cm^2 effective area for shell 1, for 2 mm and 35 mm apertures respectively, at Fe K–α, numbers obtained from the SSD continuum experiments, Chapter 11). Those at the other energies are direct measurements with the full HRMA. In Figures 12.4to12.6, which show results using the 2 mm aperture, we also show the effective area measured with the SSD continuum experiments, described more fully in Chapter 11. Continuum points below 1.3 keV have been excluded, as systematic effects dominate the measurement in this band. Note that there were both single-shell and full-HRMA measurements with 2 mm apertures at Ti K–α.

12.8 Error Analysis: FPC detectors

The quoted errors on the effective areas include several effects. Each `JMKmod` fit has uncertainties which include statistical errors and a few systematic effects which we have not corrected for.

We have included the average corrected BND fluxes $\langle F\rangle$, the RMS deviation among the four individual corrected BND fluxes δF_{dev}, the propagated fitting (including statistical) error in each BND flux δF_{prop}, and the standard deviation of the mean of the four BND fluxes, in Table 12.3 and Table 12.4.

This last quantity $\sigma_{\langle F\rangle}$ is used as the error on the BND flux for further computation, including the effective area.

$$\delta F_{dev} = \Big(\frac{1}{3}\sum_{BND}(F_{BND} - \langle F\rangle)^2\Big)^{1/2}$$

$$\delta F_{prop} = \Big(\frac{1}{4}\sum_{BND}\sigma^2_{F_{BND}}\Big)^{1/2}$$

$$\sigma_{\langle F\rangle} = \Big(\frac{1}{3\times 4}\sum_{BND}(F_{BND} - \langle F\rangle)^2\Big)^{1/2}$$

We find that the HRMA-averaged fluxes derived from the different BND-H detectors for a given test sometimes disagree in a statistically significant manner, even after correction for beam uniformity and relative quantum efficiency effects. The situation is summarized in Table 12.3 and

EE TRW ID	E (keV)	Line	Shell	$\langle F\rangle$	δF_{dev}	δF_{prop}	$\sigma_{\langle F\rangle}$	$A_{\rm eff}$
D−IXF−EE−3.001	0.277	C−Kα	1	4.273	0.154	0.035	0.077	338.143 ± 6.503
D−IXF−EE−3.012	0.277	C−Kα	1	4.438	0.025	0.037	0.012	327.784 ± 2.322
D−IXF−EE−3.002	0.277	C−Kα	3	4.310	0.037	0.035	0.019	215.486 ± 1.853
D−IXF−EE−3.013	0.277	C−Kα	3	4.449	0.030	0.036	0.015	217.122 ± 1.753
D−IXF−EE−3.003	0.277	C−Kα	4	4.265	0.063	0.035	0.032	178.157 ± 1.930
E−IXF−EE−3.014	0.277	C−Kα	4	4.070	0.037	0.034	0.018	164.369 ± 1.532
D−IXF−EE−3.004	0.277	C−Kα	6	4.269	0.041	0.035	0.021	97.197 ± 1.054
E−IXF−EE−3.015	0.277	C−Kα	6	4.066	0.032	0.033	0.016	94.222 ± 1.025
...EE−3.00[1,2,3,4]	0.277	C−Kα	sum	...	...	...	...	828.982 ± 7.111
...EE−3.01[2,3,4,5]	0.277	C−Kα	sum	...	...	...	...	803.498 ± 3.444
D−IXF−EE−4.002	0.930	Cu−Lα	all	2.198	0.029	0.025	0.014	758.110 ± 7.148
D−IXF−EE−2.001	1.486	Al−Kα	1	17.645	0.117	0.144	0.058	304.951 ± 2.042
D−IXF−EE−2.002	1.486	Al−Kα	3	36.194	0.282	0.295	0.141	203.237 ± 1.345
D−IXF−EE−2.003	1.486	Al−Kα	4	49.420	0.353	0.403	0.177	166.329 ± 1.061
D−IXF−EE−2.004a	1.486	Al−Kα	6	36.313	0.172	0.296	0.086	94.116 ± 0.581
...EE−2.00[1,2,3,4a]	1.486	Al−Kα	sum	...	...	...	...	768.633 ± 2.728
D−IXF−EE−3.005	4.510	Ti−Kα	1	19.842	0.469	0.158	0.235	103.870 ± 1.482
D−IXF−EE−3.006	4.510	Ti−Kα	3	19.926	0.489	0.159	0.244	116.448 ± 1.699
D−IXF−EE−3.007	4.510	Ti−Kα	4	19.875	0.518	0.159	0.259	103.824 ± 1.606
D−IXF−EE−3.008	4.510	Ti−Kα	6	19.920	0.507	0.159	0.253	70.427 ± 1.059
...EE−3.00[5,6,7,8]	4.510	Ti−Kα	sum	...	...	...	...	394.569 ± 2.964
E−IXF−EE−4.004	5.410	Cr−Kα	all	67.320	0.550	0.705	0.275	327.220 ± 2.464
D−IXF−EE−3.009A	6.400	Fe−Kα	3	43.304	0.506	0.585	0.253	61.867 ± 0.729
D−IXF−EE−3.010a	6.400	Fe−Kα	4	31.933	0.469	0.431	0.234	88.785 ± 1.118
D−IXF−EE−3.011	6.400	Fe−Kα	6	43.179	0.491	0.583	0.246	68.795 ± 0.797
...EE−3.0[09A,10a,11]	6.400	Fe−Kα	sum	...	...	...	...	224.146 ± 1.558
D−IXF−EE−4.001	8.030	Cu−Kα	all	43.685	2.917	1.545	1.459	82.929 ± 3.821

Table 12.3: Effective Area results for 35 mm apertures and average BND fluxes with error contributions. Note that the summed result at Fe K–α includes 4.7 ± 0.1 cm^2 for shell 1, obtained from ssd continuum measurements.

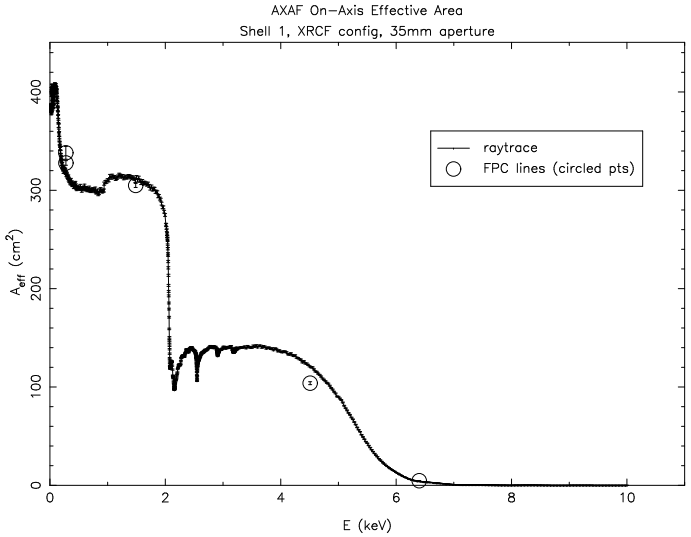

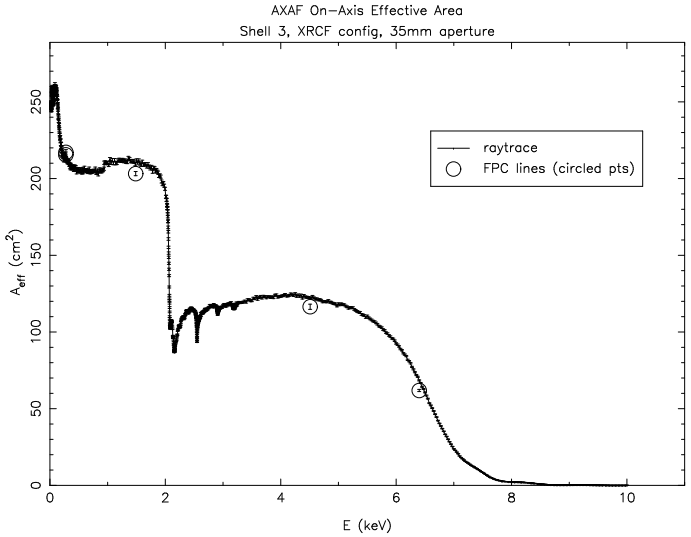

Figure 12.1: Measurements and Ray traces for effective area through 35 mm pinholes for shells 1 and 3.

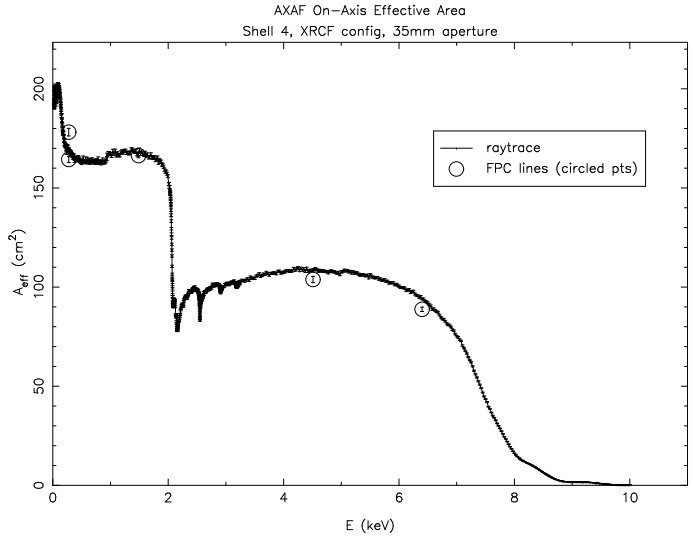

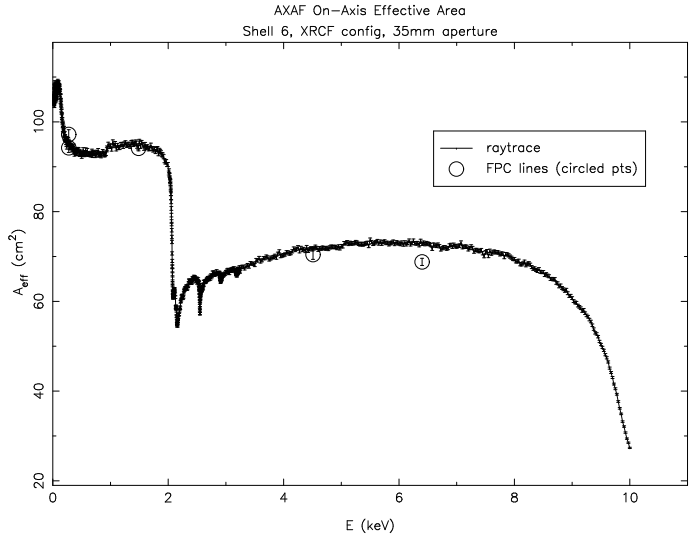

Figure 12.2: Measurements and Ray traces for effective area through 35 mm pinholes for shells 4 and 6.

EE TRW ID	E (keV)	Line	Shell	$\langle F \rangle$	δF_{dev}	δF_{prop}	$\sigma_{\langle F \rangle}$	$A_{\rm eff}$
D−IXF−EE−3.001	0.277	C−Kα	1	4.273	0.154	0.035	0.077	332.949 ± 6.407
D−IXF−EE−3.012	0.277	C−Kα	1	4.438	0.025	0.037	0.012	329.784 ± 2.351
D−IXF−EE−3.002	0.277	C−Kα	3	4.310	0.037	0.035	0.019	213.863 ± 1.837
D−IXF−EE−3.013	0.277	C−Kα	3	4.449	0.030	0.036	0.015	214.354 ± 1.725
D−IXF−EE−3.003	0.277	C−Kα	4	4.265	0.063	0.035	0.032	173.135 ± 1.883
E−IXF−EE−3.014	0.277	C−Kα	4	4.070	0.037	0.034	0.018	162.788 ± 1.540
D−IXF−EE−3.004	0.277	C−Kα	6	4.269	0.041	0.035	0.021	98.756 ± 1.082
E−IXF−EE−3.015	0.277	C−Kα	6	4.066	0.032	0.033	0.016	94.168 ± 1.028
...EE−3.00[1,2,3,4]	0.277	C−Kα	sum	...	...	...	...	818.704 ± 7.010
...EE−3.01[2,3,4,5]	0.277	C−Kα	sum	...	...	...	...	801.094 ± 3.454
D−IXF−EE−4.002	0.930	Cu−Lα	all	2.198	0.029	0.025	0.014	760.004 ± 7.163
D−IXF−EE−2.001	1.486	Al−Kα	1	17.645	0.117	0.144	0.058	294.526 ± 1.874
D−IXF−EE−2.002	1.486	Al−Kα	3	36.194	0.282	0.295	0.141	202.294 ± 1.335
D−IXF−EE−2.003	1.486	Al−Kα	4	49.420	0.353	0.403	0.177	164.509 ± 1.049
D−IXF−EE−2.004a	1.486	Al−Kα	6	36.313	0.172	0.296	0.086	92.950 ± 0.574
...EE−2.00[1,2,3,4a]	1.486	Al−Kα	sum	...	...	...	...	754.279 ± 2.593
D−IXS−MC−1.001	2.166	Nb−Lα	all	2.203	...	...	0.036	352.451 ± 5.700
E−IXS−EE−71.001	2.980	Ag−Lα	all	6.661	...	...	0.157	410.267 ± 10.066
D−IXS−EE−99.021	3.444	Sn−Lα	all	1.577	...	...	0.029	402.518 ± 8.033
D−IXF−EE−3.005	4.510	Ti−Kα	1	19.842	0.469	0.158	0.235	89.066 ± 1.280
D−IXF−EE−3.006	4.510	Ti−Kα	3	19.926	0.489	0.159	0.244	113.921 ± 1.659
D−IXF−EE−3.007	4.510	Ti−Kα	4	19.875	0.518	0.159	0.259	100.747 ± 1.556
D−IXF−EE−3.008	4.510	Ti−Kα	6	19.920	0.507	0.159	0.253	67.477 ± 1.016
D−IXF−3D−9.001	4.510	Ti−Kα	all	12.670	0.327	0.153	0.163	362.434 ± 5.688
...EE−3.00[5,6,7,8]	4.510	Ti−Kα	sum	...	...	...	...	371.211 ± 2.801
E−IXF−EE−4.004	5.410	Cr−Kα	all	68.016	0.834	0.712	0.417	307.146 ± 2.700
D−IXF−EE−3.009A	6.400	Fe−Kα	3	43.304	0.506	0.585	0.253	58.346 ± 0.691
D−IXF−EE−3.010a	6.400	Fe−Kα	4	31.933	0.469	0.431	0.234	82.246 ± 1.042
D−IXF−EE−3.011	6.400	Fe−Kα	6	43.179	0.491	0.583	0.246	64.605 ± 0.753
...EE−3.0[09A,10a,11]	6.400	Fe−Kα	sum	...	...	...	...	209.307 ± 1.463
D−IXF−EE−4.001	8.030	Cu−Kα	all	43.685	2.917	1.545	1.459	76.331 ± 3.519

Table 12.4: Effective Area results for 2 mm apertures, and average BND fluxes with error contributions. Note that the summed result at Fe K–α includes 4.1 ± 0.1 cm^2 for shell 1, obtained from ssd continuum measurements.

Table 12.4. The cause of this discrepancy is currently not understood. The comparison between δF_{dev} and δF_{prop} shows that they are in general comparable (as they should be if the dominant error is statistical), with the notable exception of Ti K–α.

12.9 SSD Data Analysis

There were three measurements of the HRMA effective area using spectral lines and the solid state detectors, with 2 mm apertures. These are listed in Table 12.1; they have TRW ID numbers containing the string "IXS" ("I"maging test (*i.e.* no gratings), with the H"X"DS, "S"SD detector). These tests were done at L-line complexes of Nb, Ag, and Sn, which in most cases would present significant challenges to FPC data analysis.

After verifying that the source is temporally stable within measurement errors, for those tests with multiple exposures, the ssd_5 spectra were summed. The data were then reduced by fitting the ssd_x and ssd_5 spectra with the `JMKmod` model, as described in Chapter 9. Great care was taken to arrive at physically reasonable values for the fitted parameters, including ratios of L-complex lines. Thanks are due to Allyn Tennant for advice on the Ag L–α fits.

Note that the use of a single beam normalization detector (ssd_5) avoids the problems discussed above with disagreements between BND fluxes. This perhaps makes the errorbars not comparable with those from the FPC tests, since this systematic effect is not present in these data.

The resulting fluxes require at least three corrections:

- Dead Time
- Beam Uniformity
- Relative Quantum Efficiency

These corrections proceed in ways analogous to those discussed above for the case of FPC detectors. A notable difference is that the beam normalization detector, ssd_5, is much closer to the source, and so beam uniformity tests must be conducted with the fpc_5 detector, and no other detector is available to control for temporal instability in the beam.

Beam uniformity factors are defined as follows:

$$BU_{\rm ssd\_5} = \frac{R(\text{fpc\_5 at ssd\_5})}{< R(\text{fpc\_5}) >_{HRMA}}.$$

In two of the cases, there exist fpc_5 beam maps done in close temporal proximity to the effective area test, and these are used. In the remaining case, Sn L–α, the high voltage for the fpc_5 was offline, so no such test was conducted. We have therefore taken beam uniformity factors from the Phase J flat field data to make this correction.

Dead time corrections are done according to the procedure outlined in Chapter 5. The initial analysis is done using the Gedcke-Hale deadtime estimates in the file headers. The pulser peak is then examined to determine how the number of counts detected compares to the number of counts injected (recorded in the file headers). The ratio of these quantities is the live time fraction. A correction factor is obtained by dividing the Gedcke-Hale live time fraction by the true value.

Relative quantum efficiency corrections are done by assuming, as shown in Chapter 11, that the ratio

$$\frac{QE(\text{ssd\_5})}{QE(\text{ssd\_x})} = 1.0141 \pm 0.0089.$$

This is not strictly correct for these low energies, especially below about 3 keV, since the ice thickness on the ssd_x window is unknown, and can have striking effects at such energies. Even so,

the 1.1% stated uncertainty on the relative quantum efficiency of the two detectors is the largest contribution to the errors of these effective area measurements.

12.10 Monochromator/FPC Effective Area Measurements

This section reports a still-in-progress analysis of the phase D and E monochromator measurements of the on-axis HRMA effective area. There are two series of measurements: the DCM measurements from phase D, and the HIREFS measurements from phase E. What follows relies on much advice from the Project Science people, especially Doug Swartz.

The HIREFS tests, which were single runs at single energies from 0.124 to 0.247 keV, have proven not very useful. This seems to be primarily because of beam uniformity problems, which are very severe due to the geometry of this monochromator; often the various BND detectors disagree as to the input flux by factors of five. This results in huge error bars. Since the beam uniformity was not in general measured at the same settings as used in the effective area tests, these data seem to be essentially worthless.

The DCM data from test D-IXF-EA-21.001 suffer from a similar problem. This test was a scan from 0.75 to 2.3 keV in steps of 50 eV. Since the strong tungsten M lines at 1.775 and 1.834 keV are in this band pass, severe beam uniformity problems resulted.

However, the situation is much better for the other 3 DCM scans, tests D-IXF-EA-2[234].001. The lack of strong tungsten lines and the broad spatially and spectrally uniform region at the HRMA entrance makes it possible to learn something from these data. All of these experiments were done with the full HRMA and 35 mm apertures. In 3 scans, they cover the range from 2.1 to 9 keV.

We have reduced the data in the usual way, fitting the FPC spectra using a `JMKmod` model consisting of no continuum, a background model (fit to background spectra and then fixed during spectral fits), and a series of spectral lines representing the first four orders of the advertised DCM energy. The first order flux only is used in the HRMA calibration. There are some interesting effects that occur in high orders when, for example, the fourth order nearly matches the tungsten L-α line; the fpc_hs sees it strongly and the other detectors do not.

We find for reasons that are not understood that the fpc_hn often disagrees with the other BND detectors as to the HRMA entrance flux; thus to minimize the error bars, it was excluded from the analysis.

We plot in Figure 12.7 the results of these analyses, using the fpc_ht, fpc_hb, and fpc_hs as normalization detectors, and making no corrections for relative quantum efficiencies or beam non-uniformities or other effects. We also show the FPC/EIPS spectral line data with 35 mm pinholes discussed above, for comparison. This plot is similar in spirit to the comparison between SSD continuum and EIPS line effective area measurements in Figure 12.6.

Several interesting effects are apparent in these data:

- The iridium M edges (the small depressions in the effective area curve between 2 and 3 keV) seem to appear in the data, just as predicted. This is of interest since other experiments (such as grating observations of the carbon continuum source) seem to indicate they are absent; while still another observation (the Nb L–α line SSD measurement discussed above) says that at least the M-IV edge is present. The presence and depths of these edge features can be used as a diagnostic of hydrocarbon contamination on the HRMA surfaces.

- The feature at 3.2 keV is almost certainly a feature of the QE of the FPC detectors, as it is coincident with the Ar K edge, at which energy the FPC QE jumps from $\sim$ 50% to unity. However, the analysis in Chapter 3 suggests that the fpc_x2 is the least sensitive of the detectors below the Ar edge, which implies that the jump in the raw effective area should go the other way:

$$A_{eff} = \frac{C_x/QE_x}{F_{BND}/ < QE >_{BND}}. \tag{12.1}$$

  Thus the effective area prior to correction for QE effects should vary inversely as the relative QE of the fpc_x2. But we observe it to jump *down* instead of the expected jump up. This effect is still under investigation.

- Some of the rattiness in the data in the 7–9 keV range is due to interaction with tungsten lines in the rotating anode source. With more care, and selection of points, this can be cleaned up a bit.

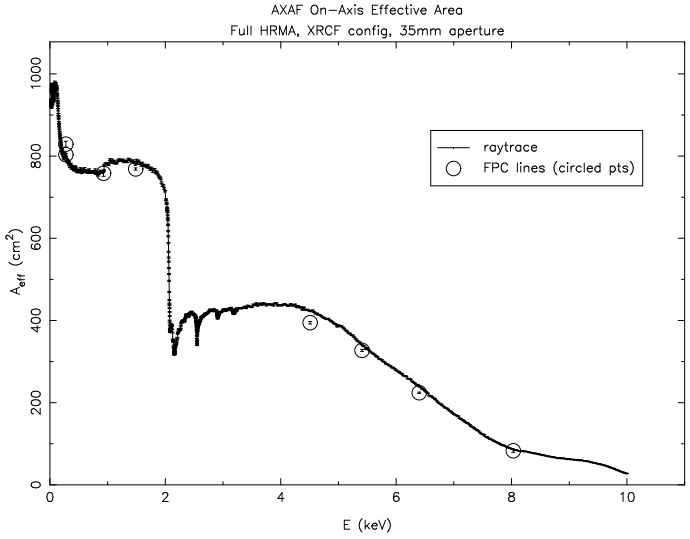

Figure 12.3: Measurements and Ray traces for effective area through 35 mm pinholes for the HRMA ensemble.

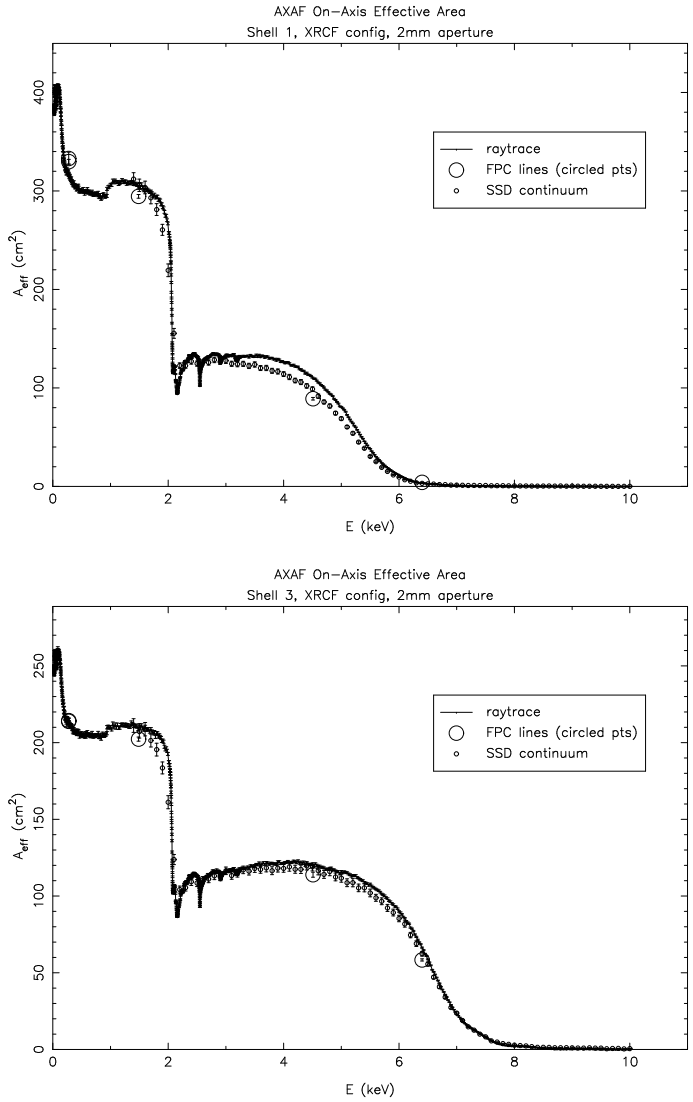

Figure 12.4: Measurements and Ray traces for effective area through 2 mm pinholes for shells 1 and 3. Both fpc_ and SSD continuum measurements are shown.

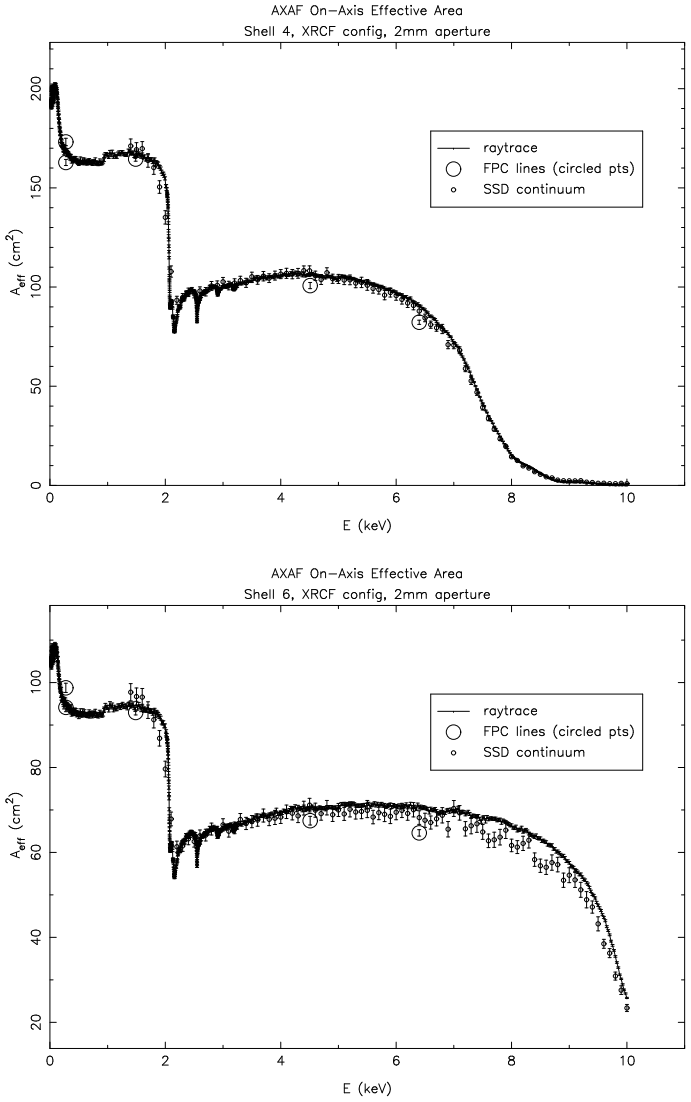

Figure 12.5: Measurements and Ray traces for effective area through 2 mm pinholes for shells 4 and 6. Both fpc_ and SSD continuum measurements are shown.

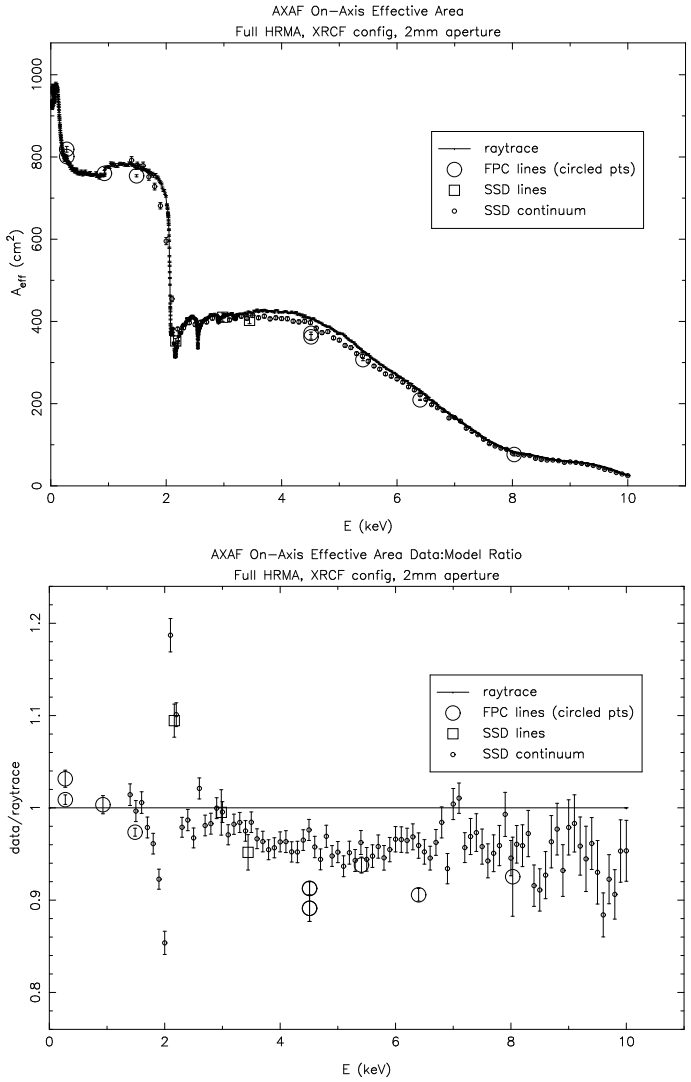

Figure 12.6: Measurements and Ray traces for effective area through 2 mm pinholes for the HRMA ensemble. Data shown include FPC and SSD line measurements and SSD continuum measurements. The lower panel shows ratios of the measurements to raytrace models.

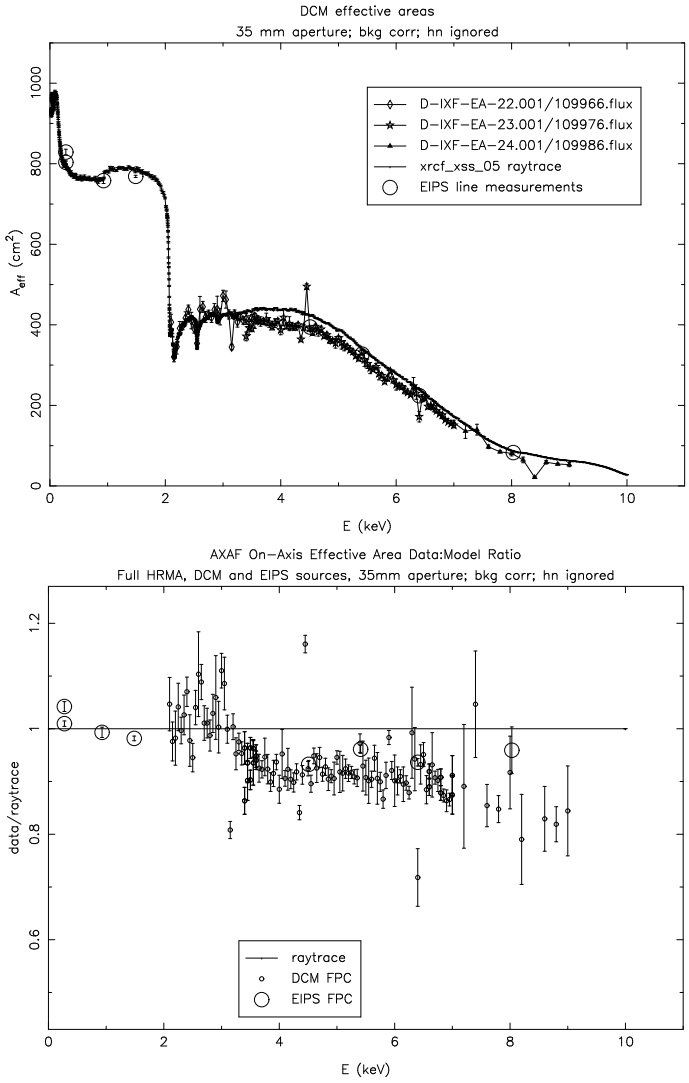

Figure 12.7: Measurements and Ray traces for effective area through 35 mm pinholes for the HRMA ensemble. Data shown include DCM measurements (small points) and FPC line measurements. The lower panel shows ratios of the measurements to raytrace models.